Estimating the Chirp Mass of Eccentric Inspiraling Binary Systems from Time-Frequency Representations of their Gravitational Radiation

Innocenzo M Pinto

University of Naples *Federico II*, INFN, LVK Collaboration
Department of Electrical Engineering and Information Technologies (DIETI),
v. Claudio 21, 80126 Napoli, Italy

E-mail: innocenzo.pinto@ligo.org

Abstract. Using the simplest yet meaningful Peters-Mathews model describing the orbital damping of a compact binary system under the emission of gravitatonal radiation, we show that the chirp-mass of an eccentric inspiraling binary, and its (Keplerian) orbital eccentricity at some reference time, can be estimated from the time-frequency skeleton of its gravitational wave signal. The estimation algorithm is nicely simple, and is robust against the non-ideal (non Gaussian, non stationary) features of detector noise.

1. Introduction

Several mechanisms exist whereby compact binary systems with large eccentricities may form [1], including close-encounters and other many-body interactions in dense stellar environments [2]-[5], and the Lidov-Kozai mechanism [6],[7]. These may result in the formation of systems with both relatively high orbital frequencies, within the observational frequency window of present-day Earth-based detectors, and large eccentricities, that wouldn't otherwise form as an effect of radiation damping alone [8].

Circular-orbit template banks are known since long to be inefficient for matched-filter detection of gravitational waves from eccentric binaries [9]-[11], due to accumulating phase-mismatch [12] resulting in large SNR loss and unacceptable false-dismissal rate; and/or eventually in selection effects, and misestimation of the source parameters [13].

Efforts to construct gravitational wave template families with eccentricity, in the time-domain and/or in the frequency domain, are ongoing following different approaches, including post-Newtonian expansions, effective-one-body models, numerical solutions, etc. - see e.g. [14]-[23]. As of today, however, no ready-to-use template family is available covering the full eccentricity range, and incorporating spin effects as well - which is needed in view of the observed degeneracy[1] between eccentricity and spin [25].

Model independent methods, based on excess-power detection in time-frequency (TF) representations [26],[27], proved effective in reconstructing injected waveforms obtained from hybrid (analytic/numeric) modeling of highly eccentric sources [28], [29]. Re-examination of

[1] Degeneracies can be circumvented, at the expense of some loss in physical insight, by orthogonalization and dimensional reduction of the parameter basis [24].

the data gathered during the 1st and 2nd observing run of the advanced LIGO and Virgo detectors, using a well tested pipeline belonging to this class [30], didn't find any signal, though, beyond those already confidently detected as originating from circular binaries [31]. Among the gravitational wave events detected by LIGO/Virgo in the O3 science-run, on the other hand, at least one (GW190521) has been indicated as possibly originating from a highly-eccentric source [32].

The possible use of TF representations for parameter estimation, other than detection of GWs from eccentric binaries was suggested in [33]-[35], and certainly deserves further investigation. It is worth noting that while the orbital phase (needed for template-based data analysis) is strongly affected by higher-order PN corrections, the orbital frequency (the main observable of TF representation based analysis) is affected to a much lesser extent.

This communication adds to the TF based approach, and proposes a simplest method for estimating the source chirp mass, and its (Keplerian) eccentricity at some reference time, using the time-frequency skeleton of its gravitational waves. For the sake of simplicity and readability, we adopt the seminal Peters-Mathews model, that makes the whole derivation straightforward (Sect. 2 and Appendix), allows to track explicitly the intensity evolution of the GW spectral lines, while they sweep the detector observational frequency-window (Sect. 3), and suggests almost naturally the proposed algorithm (Sect. 4).

2. Simplest Orbital Damping Model

The first orbital evolution model of a binary systems made of compact bodies under the emission of gravitational radiation was formulated in 1963 by J. Mathews (Caltech) and P.C. Peters (his student, at the time) [36], [37]. The relevance of the the Peters-Mathews (PM) model is threefold: historical (it supported the first indirect evidence of gravitational wave emission from continued observation of the orbital evolution of the binary pulsar PSR1913+16 [38], [39]); conceptual (all higher-order post-Newtonian models are rooted in it), and, not least, pedagogical, in view of its full mathematical solvability, and the high physical readability of the ensuing solution, describing a *universal* evolutionary scenario.

The PM analysis tracks the binary evolution starting from known initial values of the orbital frequency ω_{orb} and Keplerian orbital eccentricity e, and can be boiled down to the following equations [40] (see Appendix for details) :

$$T_c[e(0)=0] = \frac{5}{256}\omega_{orb}^{-8/3}(0)\left(\frac{c^3}{GM_\odot}\right)^{5/3}\overline{\mathcal{M}}^{-5/3} \tag{1}$$

yielding the lifetime (fiducial time to coalescence) of a circular-orbit ($e(0)=0$) binary, where $\omega_{orb}(0)$ is the orbital frequency at $t=0$, $\overline{\mathcal{M}}$ is the binary chirp-mass in solar masses, and all other symbols have the usual meaning;

$$\frac{T_c[e(0)]}{T_c(0)} = [1-e^2(0)]^4\left[1+\frac{121}{304}e^2(0)\right]^{-3480/2299}\Omega[e^2(0)] \tag{2}$$

yielding the lifetime reduction due to a non-zero initial eccentricity $e(0)\in]0,1[$, where

$$\Omega(x) = {}_2F_1\left[\frac{24}{19},\frac{3}{2},-\frac{1181}{2299},\frac{43}{19};x,-\frac{121}{304}x\right], \tag{3}$$

${}_2F_1(\cdot)$ being Appell hypergeometric function of the first kind[2];

$$\frac{\tau}{T_c[e(0)]} = 1-\left[\frac{e^2(\tau)}{e^2(0)}\right]^{24/19}\frac{\Omega[e^2(\tau)]}{\Omega[e^2(0)]} \tag{4}$$

[2] The Appell function ${}_2F_1(\cdot)$ is available, e.g., in the standard WOLFRAM MATHEMATICA® package.

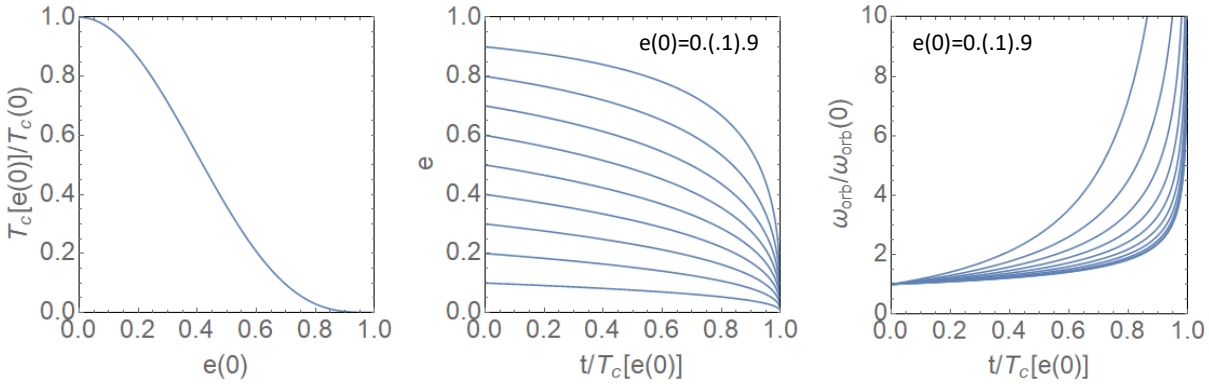

Figure 1. The PM model in a nutshell: left to right: the ratio $T_c[e(0)]/T_c(0)$ vs. $e(0)$ from eq. (2); the Keplerian eccentricity vs $t/T_c[e(0)]$, from eq. (4); the scaled orbital frequency $\omega_{orb}/\omega_{orb}(0)$ vs $t/T_c[e(0)]$, from eq. (5), for different values of $e(0)$. These curves, together with eq. (1) provide a *universal* description of binary evolution under gravitational emission.

relating (upon inversion[3]) orbital eccentricity to scaled time $t/T_c[e(0)]$, and

$$\frac{\omega_{orb}(t)}{\omega_{orb}(0)} = \left[\frac{e(t)}{e(0)}\right]^{-18/19} \left[\frac{1-e^2(t)}{1-e^2(0)}\right]^{3/2} \left[\frac{1+\frac{121}{304}e^2(t)}{1+\frac{121}{304}e^2(0)}\right]^{-1305/2299} \tag{5}$$

relating $\omega_{orb}(t)$ and $e(t)$ throughout the binary lifetime[4]. Equations (1) to (5) provide a simple, general and readable description of binary evolution under gravitational radiation, illustrated in Figure 1.

3. Gravitational Waves from Eccentric Binaries

The steady-state gravitational wave luminosity spectrum of an elliptical-orbit binary was also first derived in [36], and further elaborated in [42]-[44]. The luminosity of the n-th harmonic of the orbital frequency (sum over both polarizations) can be accordingly written

$$\mathcal{L}_n = \Pi\, \overline{\mathcal{M}}^{10/3} \left(\frac{\omega_{orb}(t)}{\omega_{orb}(0)}\right)^{10/3} g_{tot}(n,e), \tag{6}$$

where $\Pi = (32/5)G^{7/3}c^{-5}\,(M_\odot\omega_{orb}(0))^{10/3}$ (erg/sec), and

$$\begin{aligned} g_{tot}(n,e) = \frac{n^4}{32}\Bigg\{ &\Big[J_{n-2}(ne) - J_{n+2}(ne) - 2e\,[J_{n-1}(ne) - J_{n+1}(ne)] + \frac{2}{n}J_n(ne)\Big]^2 + \\ &+ (1-e^2)\,[J_{n-2}(ne) - 2J_n(ne) + J_{n+2}(ne)]^2 + \frac{4}{3n^2}J_n^2(ne)\Bigg\}. \end{aligned} \tag{7}$$

[3] The function $\Omega(x)$ is strictly monotonic in $[0,1[$, and numerical inversion of (4) is straightforward to any desired accuracy.

[4] Note that in the asymptotic circular-orbit limit, $e \sim e(0) \sim 0$, $\Omega(x) \sim 1$, $T_c[e(0)] \sim T_c(0)$, $1 - t/T_c(0) \sim [e(\tau)/e(0)]^{48/19}$, and, from eq. (5),

$$\omega_{orb}(t) \sim \omega_{orb}(0)\left(1 - \frac{t}{T_c(0)}\right)^{-3/8}.$$

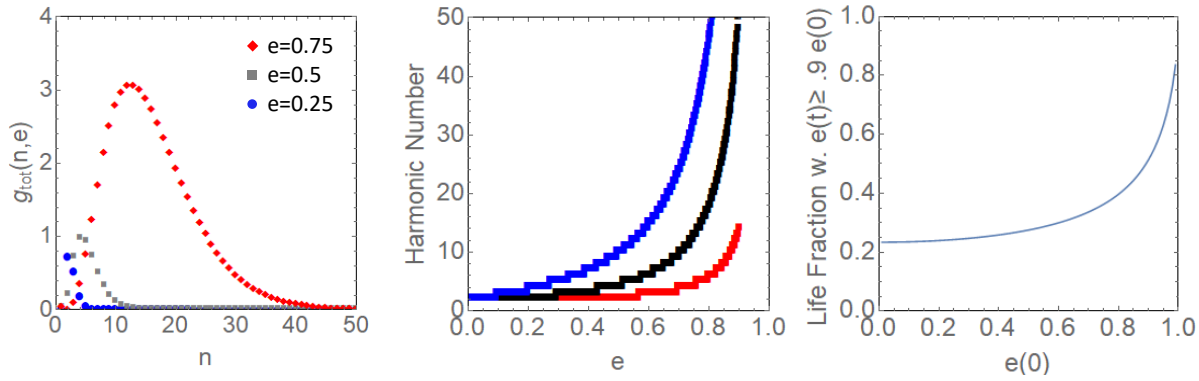

Figure 2. Left to right: steady state gravitational wave luminosity spectrum $g_{tot}(n, e)$ for three different values of e, from eq. (7); harmonic-order of the strongest line in the steady-state spectrum (black) and of the lowest (red) and highest (blue) frequency lines such that $\mathcal{L}_n \geq 0.1\mathcal{L}_{max}$, vs. orbital eccentricity; fraction of the binary lifetime where $e(t) \geq 0.9e(0)$ as a function of $e(0)$.

$J_n(\cdot)$ being the Bessel function of the first kind[5].

The function $g_{tot}(n, e)$ is shown in Figure 2 for different values of e.

It is seen that as Keplerian eccentricity increases, the order of the strongest harmonic in the spectrum and the spectral width also increase.

A non-trivial consequence of eq.s (2) and (4) is that while the binary lifetime is a decreasing function of $e(0)$, the *fraction* of the binary lifetime over which $e(t) \approx e(0)$ is an increasing function of $e(0)$, as shown in Figure 2.

It is possible to combine eq. (7) with eqs. (4) and (5) allowing to express the orbital eccentricity and frequency as functions of (scaled) time $t/T_c[e(0)]$, to see how the spectral lines and their luminosities evolve during the binary lifetime[6].

Doing so, we should keep in mind that GW data from interferometric detectors are *pass-banded*, in order to get rid of the technical noises [45] occurring below and above some typical frequencies, denoted here as f_{in} and f_{out}. Hence, the n-th spectral line will become visible (provided its luminosity exceeds the noise-floor of the detector) only in the time interval where $f_{in} \leq f_n(t) \leq f_{out}$.

In general, different harmonics will be dominant in different time-intervals, until the $n = 2$ line will take the lead, and higher harmonics will eventually vanish as $t/T_c[e(0)] \to 1$, because of asymptotic orbit circularization, for any $e(0) \in]0, 1[$. The higher harmonics, however will exceed, or remain comparable to, the 2nd one throughout a fraction of the binary lifetime that increases with $e(0)$. To illustrate the above, we consider two sources[7] with $e(0) = 0.75$ and $e(0) = 0.25$, respectively, $f_{orb}(0) = 1$Hz for both, and assume $f_{in} = 20$Hz, $f_{out} = 150$Hz. In Figure 3 all harmonics for which $\mathcal{L}_n \geq 0.01\mathcal{L}_{max}$ at $t = 0$ are included, as they sweep through the spectral window (f_{in}, f_{out}). It is seen that a bunch of higher harmonics of the more eccentric source falls in the detector spectral window already at $t = 0$; the situation is different for the less eccentric source, whose spectral lines enter the observational window much later.

[5] Efficient computational tools for evaluating the Bessel functions in eq. (7) were first discussed in [44].

[6] For simulation purposes, the evolving transverse-traceless components of the emitted gravitational waves from [37],[44] can be consistently computed using the orbital phase evolution equations derived in [12].

[7] By suitable choice of their chirp masses, these two sources can be designed using eqs. (1) and (2) to have the same lifetime. Their luminosities will be different, though, according to eq. (6).

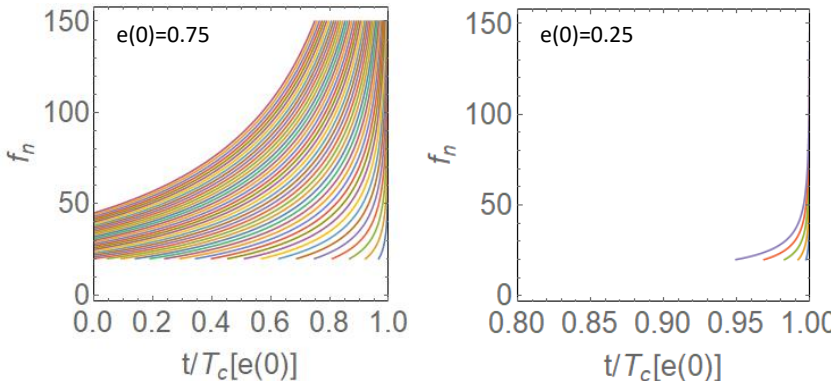

Figure 3. Frequency evolution of gravitational wave lines (harmonics of the orbital frequency) for which $\mathcal{L}_n \geq 0.01\mathcal{L}_{max}$ at $t = 0$, as they sweep the detector observational frequency window (here between 20Hz and 150Hz). Left: source with $e(0) = 0.75$; right: source with $e(0) = 0.25$; $f_{orb}(0) = 1$Hz for both sources.

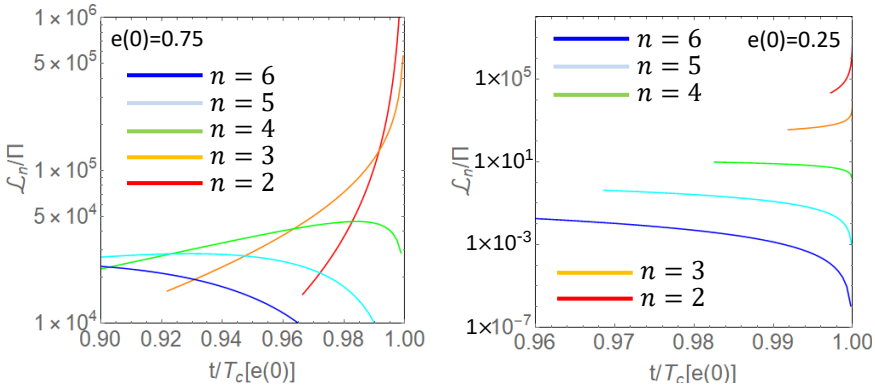

Figure 4. Evolution of the luminosity of the five strongest gravitational wave lines (harmonics of the orbital frequency) in the lifetime fraction where they sweep the detector observational freuency window (here from 20Hz to 150Hz). Left: source with $e(0) = 0.75$; right: source with $e(0) = 0.25$; $f_{orb}(0) = 1$Hz for both sources.

In Figure 4 the luminosity of the five most intense spectral lines in the late evolutionary phase is shown, again for both cases. It is seen that for the source with $e(0) = 0.25$, all harmonics with $n > 2$ are fainter by a factor $\sim 10^3$ compared to the 2nd one, throughout the interval where they sweep through the detector spectral window, between $f_{in} = 20$Hz and $f_{out} = 150$Hz; for the source with $e(0) = 0.75$, one or more of the higher harmonics exceed, or are comparable to, the asymptotically dominant 2nd one over extended fractions of the lifetime.

We may thus expect a fairly richer time-frequency scenario, compared to the simplest circular-orbit case, when observing binaries with relatively large eccentricities.

3.1. Time-Frequency Representations

Time-frequency (TF) representations aim at displaying the energy content of nonstationary signals as a function of time *and* frequency. Many such representations have been proposed, each with its own pros and cons [46], [47]. See [48] for a comparative discussion in the context of GW data analysis.

For multi-line *chirping* GW signals, consisting of harmonically-related quasi-monochromatic signals whose frequency and amplitude change adiabatically in time, TF representations should be rated according to their ability to produce uniformly sharp, faithful and clean (devoid of, e.g., nonlinear artifacts) estimates of the time-dependent (instantaneous) frequencies of the various harmonic components throughout the time-frequency plane - such ability being ultimately limited by Gabor-Heisenberg inequality.

The instantaneous frequency lines (henceforth IFLs) form the so called *skeleton* or *ridge* of the TF representation. In practice, *discrete* TF representations are used, where at each (discrete) time, the *hottest* (or a few hottest) pixel is selected to extract the skeleton. For an eccentric binary, the skeleton will accordingly consists of different tracks spanning different time intervals, reflecting the locally dominant harmonics.

The tracks representing such harmonics can be combined into a *single* line representing the (estimated) IFL of the source orbital frequency.

In the next section we shall assign, for simplicity, a unit level to all TF pixels on the orbital IFL, and a zero level value to all other pixels[8].

4. A Simple Chirp Mass Estimator for Eccentric Sources

The PM model suggests a simple algorithm for estimating, given the orbital IFL, the chirp mass of an eccentric binary together with its (Keplerian) orbital eccentricity at some reference time[9]. The first equation in (A.1), integrated between t_1 and t_2 and combined with (A.5) can be formally solved for the normalized chirp mass $\overline{\mathcal{M}} = \mathcal{M}/M_\odot$, yielding

$$\overline{\mathcal{M}} = \left(\frac{c^3}{GM_\odot}\right)\left\{\frac{5}{256}\frac{\omega_{orb}^{-8/3}(t_1)-\omega_{orb}^{-8/3}(t_2)}{\int_{t_1}^{t_2} f[e(t)]dt}\right\}^{3/5} \quad . \tag{8}$$

From (8) we may obtain as many values of the chirp mass $\overline{\mathcal{M}}$, as the number of available TF pixel-pairs [10] $\{\{t_1,\omega_{orb}(t_1)\},\{t_2,\omega_{orb}(t_2)\}\}$ from the given orbital IFL. In the absence of noise and numerical (roundoff) errors, one would obtain from (8) the *same* value of $\overline{\mathcal{M}}$ from *all* TF pairs . In practice, the computed values of $\overline{\mathcal{M}}$ will be different, and can be binned to form a histogram, $\mathcal{D}(\overline{\mathcal{M}})$, to obtain an estimate of the source chirp-mass [49].

The computation of (8) is straightforward for circular orbits[11] where the integral in the denominator is simply $(t_2 - t_1)$. In the general case of elliptical orbits, in order to compute the integral in (8) we first need to set a time origin $t = 0$ at some (arbitrary) time-sample in the available IFL, and retrieve the corresponding $\omega_{orb}(0)$. Then, for any *trial value* of $e(0) \in [0, 1[$, we can derive an instantaneous eccentricity line (IEL) from the available IFL and the above determined $\omega_{orb}(0)$, by numerical inversion of (5), and use it to compute the integral in the denominator of (8). We may accordingly obtain a *family* of histograms corresponding to a suitable set of trial values of $e(0)$.

The results of such procedure are illustrated by examples in Table 1, and suggest the following simple algorithm for estimating *both* the chirp-mass and the Keplerian eccentricity at the reference time $t = 0$:

[8] Extension to the more general case where each TF pixel (and hence each pixel pair) has a non-binary level is straightforward, and amounts to adding the (non-unitary) levels of the pairs to the histogram bin counts.

[9] A possible choice for this latter is e.g. the time when some (visible) spectral line enters the detector spectral window.

[10] In practice, only pairs for which $|t_2 - t_1| \gg \delta_t$ and $|\omega_{orb}(t_2) - \omega_{orb}(t_2)| \gg \delta_\omega$ should be used, δ_t, δ_ω being the time and frequency resolution of the available TF representation.

[11] Note that retrieving the chirp mass from the IFL via eq. (8) does *not* require differentiation of the IFL, at variance of the conceptually similar method proposed in [34].

Table 1. Retrieving the chirp mass from eccentric inspirals, using eq. (8). Two illustrative examples are considered: left: $\{e(0) = 0.5, \overline{\mathcal{M}} = 2.8\}$, and right: $\{e(0) = 0.1, \overline{\mathcal{M}} = 30\}$. We use noise-free one-bit coded orbital IFLs, and a typical number of time-frequency TF pixel pairs $\sim 5{\cdot}10^3$. The quantities $\widehat{\overline{\mathcal{M}}}$ and $\widehat{\sigma}$ are the median and std. deviation of the chirp mass histograms computed from eq. (8) for various values of $e(0)$. For both examples $t = 0$ was chosen as the time when the 2nd harmonic of the orbital frequency enters the detector observational frequency window at $f_{in} = 20$Hz. The trial value e_k that most closely matches the true (unknown) $e(0)$ is signaled by minima in both the spread ($\widehat{\sigma}$) and the L^2 error between the actual IFL and the one reconstructed from the trial eccentricity and the corresponding estimated chirp mass.

e_k	$\widehat{\overline{\mathcal{M}}}$	$\widehat{\sigma}$	L^2 error
0.1	4.94	0.78	1.81
0.15	4.84	0.72	1.68
0.2	4.69	0.65	1.46
0.25	4.49	0.55	1.07
0.3	4.25	0.45	0.56
0.35	3.95	0.33	1.42
0.4	3.61	0.22	2.32
0.45	3.22	0.11	1.90
0.5	**2.80**	**0.02**	**0.45**
0.55	2.37	0.05	0.52
0.6	1.94	0.10	0.85
0.65	1.52	0.13	1.04
0.7	1.14	0.14	1.16
0.75	0.80	0.12	1.24
0.8	0.51	0.09	1.31

e_k	$\widehat{\overline{\mathcal{M}}}$	$\widehat{\sigma}$	L^2 error
0	30.65	0.23	0.06
0.025	30.61	0.21	0.05
0.05	30.49	0.17	0.04
0.075	30.29	0.11	0.02
0.1	**30.00**	**0.02**	**0.00**
0.125	29.63	0.10	0.02
0.15	29.17	0.23	0.04
0.175	28.64	0.38	0.06
0.2	28.02	0.55	0.08
0.225	27.31	0.73	0.11
0.25	26.53	0.92	0.17
0.275	25.67	1.11	0.24
0.3	24.73	1.30	0.31
0.325	23.72	1.48	0.38
0.35	22.64	1.66	0.44

(i) construct the histograms $\mathcal{D}_k(\overline{\mathcal{M}})$ corresponding to a set of possible values $\{e_k | k = 1, 2, \ldots, N\}$ of $e(0)$ in $[0, 1[$, and let $\widehat{\overline{\mathcal{M}}}_k$ the corresponding chirp-mass estimate (e.g., the median), and Δ_k the L^2 error between the available orbital IFL and the *reconstructed* IFL obtained by letting $\{e(0), \overline{\mathcal{M}}\} = \{e_k, \widehat{\overline{\mathcal{M}}}_k\}$;

(ii) find k for which $\mathcal{D}_k(\overline{\mathcal{M}})/\Delta_k$ has the highest peak, and take $\{e_k, \widehat{\overline{\mathcal{M}}}_k\}$ as your estimate of the source parameters.

The different heights of the histogram peaks resolve the estimation ambiguity originating from the degeneracy between chirp mass and eccentricity pointed out in [51] and further discussed in [52],[53]. An example of the histogram family obtained using simulated data added to a stretch of (public domain) LIGO noise is shown in Figure 5.

4.1. Robustness

A quantitative assessment of the impact of noise in the data in terms of bias and spread of the obtained estimates is in progress, based on massive numerical simulations.

Additive locally stationary/Gaussian noise in the data manifests itself in the 1-bit coded TF skeleton as frequency *jitter*, whereby $\omega_{orb}(t_n)$ may be slightly different from its true/expected value.

More interesting is the case where strong transients of untraced environmental/instrumental

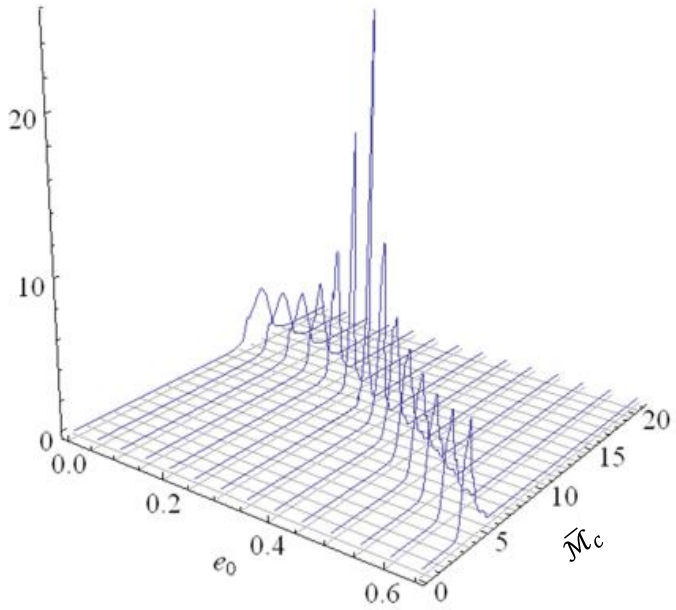

Figure 5. The weighted histogram $\mathcal{D}_k(\overline{\mathcal{M}})/\Delta_k$ for an eccentric inspiral with $e(0) = 0.3$ and $\overline{\mathcal{M}} = 12.16$ (courtesy P. Addesso [50]). The waveform was generated using [12] and [44] and added to a stretch of (public domain) LIGO background noise for an $SNR = 25dB$. The TF representation used to produce the orbital IFL was a sparsified smoothed Wigner-Ville [48].

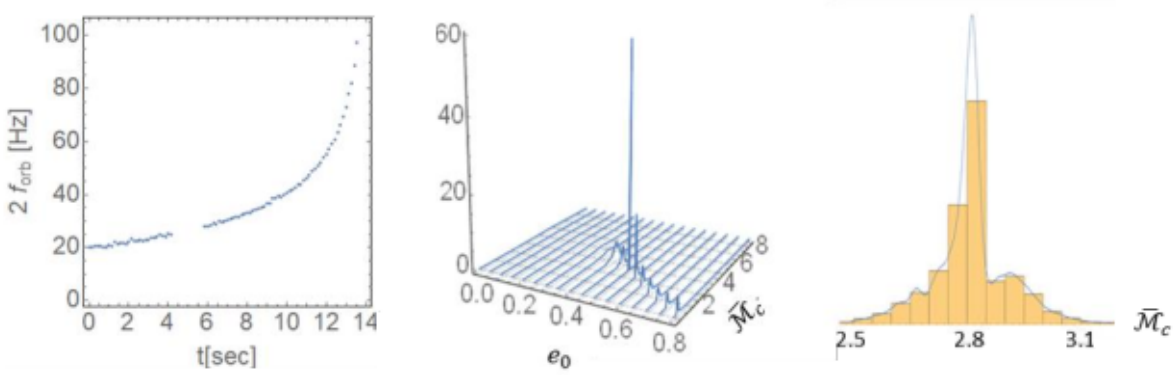

Figure 6. Left: noisy one-bit encoded IFL with excision. Source parameters: $e(0) = 0.5, \overline{\mathcal{M}} = 2.8$. The shown jitter corresponds roughly to an (energy) SNR ~ 20 in the simulated data; center: the corresponding family of smoothed histograms $\mathcal{D}_k/\Delta_k$; right: a close-up of the smoothed and raw $e_k = 0.5$ histogram; a tiny second lobe is visible.

origin (nicknamed *glitches*) are present. These should be excised from the data, yielding a *lacunary* IFL. Preliminary results indicate that the poposed algorithm is nicely robust against both kinds of noises above. Qualitatively, the main effect of IFL jitter is to *broaden the peaks* of the $\overline{\mathcal{D}}_k$ histograms; the main effect of lacunarity is to produce moderate *multi-modality* in the histograms, as illustrated in Figure 6.

5. Conclusions

The PM binary evolution model may be deemed as exceedingly simple to describe a realistic binary system, where e.g., higher order post-Newtonian corrections, spin and precession effects, may be important. However, it provides a neat conceptual framework that may be used as a guideline to build more sophisticated, yet readable and predictive, investigations.

In addition, it suggests a simple and nicely informative algorithm for estimating the source chirp mass and the Keplerian eccentricity at some reference time from the TF skeleton of the gravitational wave data, useful to restrict a full fledged template-based analysis, whose computational burden would be otherwise unaffordable, to a suitably reduced subset of the whole source parameter space.

Acknowledgements

The author acknowledges several useful discussions with V. Pierro, P. Addesso, V. Matta, A. Fusco, E. Mejuto-Villa and G.C. Cella. Special thanks go to the PIRT-21 Organizers and the whole Conference Staff.
This work is dedicated to the memory of Theo Demma.

Appendix

The Peters-Mathews equations ruling two compact (point) masses in a Keplerian orbit are:

$$\begin{cases} \langle \dfrac{da}{dt} \rangle = -\dfrac{64}{5}\dfrac{G^3}{c^5}\dfrac{m_1 m_2 (m_1+m_2)}{a^3(1-e^2)^{7/2}}\left(1+\dfrac{73}{24}e^2+\dfrac{37}{96}e^4\right) \\ \langle \dfrac{de}{dt} \rangle = -\dfrac{304}{15}\dfrac{G^3}{c^5}\dfrac{m_1 m_2 (m_1+m_2)}{a^4(1-e^2)^{5/2}}\left(1+\dfrac{121}{304}e^2\right)e \end{cases} \tag{A.1}$$

where a and e are the (Keplerian) orbital semimajor axis and eccentricity, $m_{1,2}$ the companion masses, and $\langle\cdot\rangle$ denotes averaging over an orbit. Equations (A.1) are obtained from conservation of energy and angular momentum, after using the quadrupole gravitational radiation formula. They are valid to lowest meaningful order in the usual v/c and r_g/r parameters, r_g being the binary gravitational radius, and under the assumption that the orbital parameters change adiabatically, viz., $T(d/dt)\log(T) \ll 1 \wedge T(d/dt)\log(e) \ll 1$. Using Kepler law relating the semimajor axis to the orbital frequency,

$$a(t) = \omega_{orb}^{-2/3}[G(m_1+m_2)]^{1/3} \tag{A.2}$$

equations (A.1) can be written

$$\begin{cases} \dfrac{d}{dt}\left[\dfrac{\omega_{orb}(t)}{\omega_{orb}(0)}\right]^{-8/3} = -\dfrac{f[e(t)]}{T_c(0)} \\ \dfrac{de}{dt} = -\left[\dfrac{\omega_{orb}(t)}{\omega_{orb}(0)}\right]^{8/3}\dfrac{19}{48}\dfrac{g[e(t)]}{T_c(0)} \end{cases} \tag{A.3}$$

where

$$f(e) = (1-e^2)^{-7/2}\left(1+\frac{73}{24}e^2+\frac{37}{96}e^4\right),\ g(e) = (1-e^2)^{-5/2}\left(1+\frac{121}{304}e^2\right)e \tag{A.4}$$

and

$$T_c(0) = \frac{5}{256}\omega_{orb}^{-8/3}(0)\left(\frac{c^3}{GM_\odot}\right)^{5/3}\mathcal{M}^{-5/3} \tag{A.5}$$

$\overline{\mathcal{M}}$ being the binary chirp mass in units of $M_\odot$, and all other symbols having the usual meaning. If $e(0) = 0$, it is seen that $e(t) = 0, \forall t$, and the first equation in (A.3) yields

$$\omega_{orb}(t) = \omega_{orb}(0)\left(1 - \frac{t}{T_c(0)}\right)^{-3/8} \tag{A.6}$$

whereby $T_c(0)$ is understood as the fiducial binary *lifetime* for a circular orbit, i.e., the time until the orbit radius vanishes ($a = 0$). We shall denote as $T_c[e(0)]$ the binary lifetime for the general case of non-zero initial eccentricity. If $e(0) \neq 0$ the two equations in (A.3) can be combined to obtain

$$\frac{d}{de}\log\left[\frac{\omega_{orb}(t)}{\omega_{orb}(0)}\right]^{-8/3} = \frac{48}{19}\frac{f[e(t)]}{g[e(t)]} \tag{A.7}$$

which is readily integrated, yielding the following relationship between $e(t)$ and $\omega_{orb}(t)$, valid throughout the binary lifetime.

$$\frac{\omega_{orb}(t)}{\omega_{orb}(0)} = \left[\frac{e(t)}{e(0)}\right]^{-18/19}\left[\frac{1-e^2(t)}{1-e^2(0)}\right]^{3/2}\left[\frac{1+\frac{121}{304}e^2(t)}{1+\frac{121}{304}e^2(0)}\right]^{-1305/2299} \tag{A.8}$$

This can used in (A.3) to obtain

$$\frac{de}{dt} = -\frac{19}{48}\left[\frac{e(t)}{e(0)}\right]^{-48/19}\left[\frac{1-e^2(t)}{1-e^2(0)}\right]^{4}\left[\frac{1+\frac{121}{304}e^2(t)}{1+\frac{121}{304}e^2(0)}\right]^{-3480/2299}\frac{g[e(t)]}{T_c(0)}. \tag{A.9}$$

This latter can be integrated between $t = \tau$ and the coalescency time $t = T_c[e(0)]$, where the eccentricity vanishes,

$$\begin{aligned}\frac{T_c[e(0)]-\tau}{T_c(0)} = \frac{48}{19}[e(0)]^{-48/19}[1-e^2(0)]^4\left[1+\frac{121}{304}e^2(0)\right]^{-3480/2299}\cdot \\ \cdot\int_0^{e(\tau)} e^{29/19}[1-e^2]^{-3/2}\left[1+\frac{121}{304}e^2\right]^{1181/2299}de.\end{aligned} \tag{A.10}$$

Upon letting $e^2 = xe^2(\tau)$, the integral on the r.h.s. of (A.10) becomes

$$\frac{[e(\tau)]^{48/19}}{2}\int_0^1 x^{5/19}[1-xe^2(\tau)]^{-3/2}\left[1+\frac{121}{304}xe^2(\tau)\right]^{1181/2299}dx, \tag{A.11}$$

that is expressible in terms of P.E. Appell's generalized hypergeometric function of the first kind ([41], eq. 3.211). Hence:

$$\frac{T_c[e(0)]-\tau}{T_c(0)} = \left[\frac{e(\tau)}{e(0)}\right]^{48/19}[1-e^2(0)]^4\left[1+\frac{121}{304}e^2(0)\right]^{-3480/2299}\Omega[e^2(\tau)]. \tag{A.12}$$

where

$$\Omega(x) = {}_2F_1\left[\frac{24}{19},\frac{3}{2},-\frac{1181}{2299},\frac{43}{19};x,-\frac{121}{304}x\right]. \tag{A.13}$$

For $\tau = 0$ this becomes

$$\frac{T_c[e(0)]}{T_c(0)} = [1-e^2(0)]^4\left[1+\frac{121}{304}e^2(0)\right]^{-3480/2299}\Omega[e^2(0)] \tag{A.14}$$

whereby (A.12) can be further written,

$$\frac{\tau}{T_c[e(0)]} = 1 - \left(\frac{e^2(\tau)}{e^2(0)}\right)^{24/19} \frac{\Omega[e^2(\tau)]}{\Omega[e^2(0)]}. \tag{A.15}$$

Equations (A.5), (A.8), (A.14) and (A.15) are the general exact solution of PM equations, first obtained in [40].

As stressed in Sect. 1, this solution is both computationally cheap and numerically accurate.

References

[1] Tagawa H *et al* 2021 *Astrophys. J. Lett.* **907** L20
[2] Gondan L *et al* 2018 *Astrophys J.* **860** 5
[3] Samsing J 2018 *Phys. Rev.***D97** 103014
[4] Gold *et al Phys. Rev.* **D 86** 121501(R)
[5] Vick M and Lai D 2019 *Phys. Rev.* **D100** 063001
[6] Naoz S 2016 *Ann. Rev. Astron. Astroph.* **54** 441
[7] Liu B *et al* 2019 *Astrophys. J.* **881** 41
[8] Kowalska I *et al* 2010 *Astronomy & Astrophys.* **527** A70
[9] Martel E K and Poisson E, 1999 *Phys. Rev.* **D60** 124008
[10] Brown D A and Zimmermann P J 2010 *Phys. Rev.* **D81** 024007
[11] Favata M *et al* 2014 *Phys. Rev. Lett.* **112** 101101
[12] Pierro V and Pinto I M 1996 *Nuovo Cimento* **B111** 1517
[13] Ramos Buades A *et al* (2020) *Phys. Rev.* **D101** 083015
[14] Damour T *et al* 2004 *Phys. Rev.* **D70** 064028
[15] Moore B *et al* 2016 *Phys. Rev.* **D 93** 124061
[16] Tanay S *et al* 2016 *Phys. Rev.* **D93** 064031
[17] Huerta E *et al* 2018 *Phys. Rev.* **D97** 024031
[18] Csizmadia *et al* 2012 *Class. Quantum Grav.* **29** 245002
[19] East W *et al* 2013 *Phys. Rev.* **D87** 043004
[20] Hinderer T and Babak S 2017 *Phys. Rev.* **D96** 104048
[21] Cao Z and Han W B 2017 *Phys. Rev.* **D96**
[22] Liu X *et al* 2020 *Phys. Rev.* **D101** 044049
[23] Chiaramello D and Nagar A 2020 *Phys. Rev.* **D101** 101501(R)
[24] Barta D. and Vasúth M 2018 *Phys. Rev.* **D97** 124011
[25] Romero-Shaw I. *et al* 2020 *Astrophys J. Lett.* **903** L5
[26] Klimenko S *et al* 2008 *Class. Quantum Grav.* **25** 114029
[27] Cornish N J *et al* 2021 *Phys. Rev.* **D103** 044006
[28] Tai K-S *et al* 2014 *Phys. Rev.* **D90** 103001
[29] Dalya G *et al* 2021 *Class. Quantum Grav.* f38 065002
[30] Klimenko S *et al* 2016 *Phys. Rev.* **D93** 042004
[31] Abbott B P *et al* 2019 *Astrophys. J.* **883** 149
[32] Gayathry V *et al* 2020 *preprint* ArXiV:2009:05461
[33] Coughlin M *et al* 2015 *Phys. Rev.* **D91** 063004
[34] Tiwari V *et al* 2016 *Class. Quantum Grav.* **33** 01LT01
[35] Tiwari V *et al* 2016 *Phys. Rev.* **D93** 043007
[36] Peters P C and Mathews J 1963 *Phys. Rev.* **131** 435
[37] Peters P C 1964 *Phys. Rev.* **136** B1224
[38] Taylor J H and Weisberg J M 1982 *The Astrophysical Journal* **253** 908
[39] Weisberg J M and Huang Y 2016 *The Astrophysical Journal* **829** 55
[40] Pierro V and Pinto I M 1996 *Nuovo Cimento* **B111** 631
[41] Gradshteyn I S and Ryzhik I M 1980 *Tables of Integrals Series and Products* (New York, NY : Academic Press)
[42] Zel'dovich Ya B and Novikov I N 1967 *Relativistic Astrophysics*, vol. 1, sect. 1.13 (Chicago, IL : Chicago Univ. Press)
[43] Moreno-Garrido C *et al* 1994 *Mon. Not. Roy. Astron. Soc.* **266**16; ibid. 1995 **274** 115
[44] Pierro V *et al* 2001 *Mon. Not. Roy. Astron. Soc.* **325** 358; ibid. 2002 **334** 855
[45] Martynov D V *et al* 2016 *Phys. Rev* **D93** 112004; ibid. 2018 **D97** 059901
[46] Boashash B B 2016 *Time-Frequency Signal Analysis and Processing*, (New York, NY : Academic Press)

[47] Flandrin P 1998 *Time-Frequency/Time-Scale Analysis*, (New York, NY : Academic Press)
[48] Addesso P *et al* 2016 *preprint* arXiv:1605.03496
[49] Mejuto-Villa E 2019 *PhD Thesis* (Benevento: University of Sannio)
[50] Addesso P *et al* 2021 LIGO Document G2100118
[51] Lenon A K *et al* 2020 *Mon. Not. Roy. Astron. Soc.* **497** 1966
[52] Bose N and Pai A 2021 *preprint* arXiv:2107.14736
[53] Favata M *et al* 2021 *preprint* arXiv:2108.05861